



CHORUS

This is the accepted manuscript made available via CHORUS. The article has been published as:

Tricritical point and phase diagram based on critical scaling in the monoaxial chiral helimagnet $\text{Cr}_{\{1/3\}}\text{NbS}_{\{2\}}$

Hui Han, Lei Zhang, Deepak Sapkota, Ningning Hao, Langsheng Ling, Haifeng Du, Li Pi,
Changjin Zhang, David G. Mandrus, and Yuheng Zhang

Phys. Rev. B **96**, 094439 — Published 29 September 2017

DOI: [10.1103/PhysRevB.96.094439](https://doi.org/10.1103/PhysRevB.96.094439)

Tricritical point and phase diagram based on critical scaling in monoaxial chiral helimagnet $\text{Cr}_{1/3}\text{NbS}_2$

Hui Han,^{1,2} Lei Zhang,^{1,*} Deepak Sapkota,³ Ningning Hao,¹ Langsheng Ling,¹ Haifeng Du,¹ Li Pi,^{1,4} Changjin Zhang,¹ David G. Mandrus,^{3,5,6,†} and Yuheng Zhang^{1,4}

¹*High Magnetic Field Laboratory, Chinese Academy of Sciences, Hefei 230031, China*

²*University of Science and Technology of China, Hefei 230026, China*

³*Department of Physics and Astronomy,*

The University of Tennessee, Knoxville, Tennessee 37996, USA

⁴*Hefei National Laboratory for Physical Sciences at the Microscale,
University of Science and Technology of China, Hefei 230026, China*

⁵*Materials Science and Technology Division,*

Oak Ridge National Laboratory, Oak Ridge, Tennessee 37831, USA

⁶*Department of Materials Science and Engineering,*

The University of Tennessee, Knoxville, Tennessee 37996, USA

Abstract

In this work, the magnetism of the single crystal $\text{Cr}_{1/3}\text{NbS}_2$, which exhibits chiral magnetic soliton lattice (CSL) state, is investigated. The magnetization displays strong magnetic anisotropy when the field is applied perpendicularly and parallel to the c -axis in low field region ($H < H_S$, H_S is the saturation field). The critical exponents of $\text{Cr}_{1/3}\text{NbS}_2$ are obtained as $\beta = 0.370(4)$, $\gamma = 1.380(2)$, and $\delta = 4.853(6)$, which are close to the theoretical prediction of three-dimensional Heisenberg model. Based on the scaling equation and the critical exponents, the $H - T$ phase diagram in the vicinity of the phase transition is constructed, where two critical points are determined. One is a tricritical point which locates at the intersection between the CSL, forced ferromagnetic (FFM), and paramagnetic (PM) states. The other one is a critical point situated at the boundaries between CSL, helimagnetic (HM), and PM states.

PACS numbers: 75.30.Gw, 75.40.-s, 75.40.Cx

Keywords: chiral magnetic solition; helimagnetism; critical scaling; phase diagram; tricritical point

I. INTRODUCTION

Magnetic materials with chirality have attracted considerable attention due to spin-textures such as helimagnetic (HM) structure, conical magnetic ordering, magnetic skyrmion, chiral bobber¹⁻⁵. The chirality with spin-orbital coupling in the crystal structure results in an antisymmetric exchange interaction called the Dzyaloshinskii-Moriya (DM) interaction, which is 1~2 orders of magnitude weaker than the ferromagnetic coupling^{6,7}. The competition between the DM interaction with the ferromagnetic coupling causes the appearance of chiral spin-texture⁸. When an external magnetic field is applied above a threshold value, the HM ordering is usually modulated into particle-like spin-texture such as skyrmion, magnetic soliton.

Recently, the monoaxial chiral magnet $\text{Cr}_{1/3}\text{NbS}_2$ becomes prominent due to the chiral magnetic soliton lattice (CSL), which is a type of superlattice structure consist of periodic helical spin texture⁹⁻¹¹. The crystal structure for $\text{Cr}_{1/3}\text{NbS}_2$ belongs to the space group $P6_322$ ^{12,13}. The hexagonal layers in 2H-NbS₂ are intercalated by the Cr ions which are in the trivalent state with localized moments $S = 3/2$, whereas the electronic conduction originates from an unfilled band of Nb atoms. Due to the strong magnetocrystalline anisotropy and DM interaction, $\text{Cr}_{1/3}\text{NbS}_2$ displays a ground state of helical magnetic ordering with vector along the c -axis^{13,14}. The magnetic sate can be modulated differently through the direction of the applied external field. When H is applied parallel to the c -axis, the HM ordering is polarized to conical ordering, and finally to forced ferromagnetical (FFM) phase. However, when H is applied perpendicularly to the c -axis, the HM structure with 48 nm changes continuously into CSL state, which is well reproduced by the one-dimensional chiral sine-Gordon model¹⁰. Further increase of H results in a phase transition from an incommensurate CSL to a commensurate FFM state¹⁵. It has been demonstrated that CSL can be effectively manipulated by magnetic field or current injection, which supplies potential application as spintronic device¹⁶⁻¹⁸.

Although the phase transition and CSL in $\text{Cr}_{1/3}\text{NbS}_2$ have been intensively investigated, controversies emerge for the complex phase diagrams¹⁹⁻²³. The phase diagrams have been constructed in several experimental and theoretical works^{12,15,24-27}. However, vagueness and difference exist on boundaries between different phases, especially in the vicinity of the phase transition. In this work, the $H - T$ phase diagram of the single crystal $\text{Cr}_{1/3}\text{NbS}_2$ is

constructed based on the critical scaling method, where the phases and boundaries in the vicinity of the transition are clearly clarified. The critical behavior unambiguously indicates that the magnetic coupling is of a three-dimensional (3D) Heisenberg type, which suggests that the magnetic coupling of Cr-Cr occurs not only within the ab -plane but also between the interlayers along the c -axis. In addition, two critical points are determined on the $H - T$ phase diagram.

II. EXPERIMENTAL METHODS

Single crystals of $\text{Cr}_{1/3}\text{NbS}_2$ were grown by the chemical vapor transport(CVT) method using iodine as the transport agent¹³. The chemical compositions were carefully checked by Energy Dispersive X-ray(EDX) spectrometry. The crystal structure was confirmed by the Rigaku-TTR3 X-ray diffractometer using high-intensity graphite monochromatized $\text{Cu K}\alpha$ radiation. The magnetization was measured using a Quantum Design Vibrating Sample Magnetometer (SQUID-VSM). The no-overshoot mode was applied to ensure a precise magnetic field. The magnetic field was relaxed for two minutes before data collection. For the measurement of initial isothermal magnetization, the sample was firstly heated adequately above T_C for ten minutes, then cooled to the target temperature under zero magnetic field.

III. RESULTS AND DISCUSSION

Figure 1 (a) shows the crystal structure for $\text{Cr}_{1/3}\text{NbS}_2$. The NbS_2 is a quasi-two-dimensional system with van der Waals interaction between the layers. The Cr atoms are intercalated in the octahedral holes between the trigonal prismatic layers of 2H-NbS_2 ¹². Figure 1 (b) gives the morphology of the $\text{Cr}_{1/3}\text{NbS}_2$ single crystal. The single crystal presents layered characteristics, with a bright hexagonal surface of $1 \text{ mm} \times 1 \text{ mm}$. The chemical proportion is determined by the EDX spectrum as depicted in Fig. 1 (c), which gives that the proportion of Cr : Nb : S is close to 0.33 : 1 : 2. The bright surface was checked by XRD as shown in Fig. 1 (d), which indicates that the surface is (001) plane. The inset of Fig. 1 (d) presents the rock curve of the (001) diffraction peak, the full-width-at-half-maximum (FWHM) of which is $\Delta\theta = 0.071^\circ$. The single peak and narrow FWHM of the rock curve indicate high quality of the single crystal sample without twin crystal. The XRD pattern of

the single crystal gives the lattice constant $c = 12.029(8) \text{ \AA}$, which is very close to previous reports^{13,14,28}.

Figure 2 (a) and (b) gives the temperature dependence of magnetization $[M(T)]$ under selected field, where the external field is applied perpendicularly and parallel to the c -axis respectively. All $M(T)$ curves with $H \perp c$ or $H//c$ undergo a magnetic ordering transition at the phase transition temperature $T_C \sim 125 \text{ K}$, which is in agreement with previous report¹³. However, the $M(T)$ curves exhibit different behaviors when $H \perp c$ and $H//c$. When $H \perp c$, $M(T)$ curves below $H = 500 \text{ Oe}$ almost display the same behavior, as shown in Fig. 2 (a). However, when H exceeds 500 Oe , the values under fixed field increase abruptly. On the other hand, when $H//c$, $M(T)$ curves are raised monotonously with the applied field, as presented in Fig. 2 (b). These different behaviors of $M(T)$ between $H \perp c$ and $H//c$ can be attributed to the formation of CSL^{13,14}. When $H \perp c$, the CSL forms under the lower field, thus the $M(T)$ curves exhibit similar behaviors in the CSL phase. However, when under higher field, the CSL is destroyed abruptly, which causes the prominent different behaviors in $M(T)$ curves. When $H//c$, no CSL phase forms but a conical ordering is polarized gradually. Therefore, no abrupt change appears in the $M(T)$ curves when $H//c$. In addition, it is also noticed from the insets of Fig. 2 that bifurcations occur to the zero-field-cooling (ZFC) and field-cooling (FC) curves, which are attributed to the different magnetic ground state under zero field and non-zero-field. As we know, the HM is polarized to conical spin ordering by the external field. In a sequence of ZFC, the system exhibits a HM ordering, where the HM ordering is gradually polarized by the field with the increase of temperature. However, In a sequence of FC, the system displays a ground state of conical ordering. Thus, the different magnetic ground states under zero-field and non-zero-field result in the different behaviors between ZFC an FC curves^{13,14}.

As indicated by the $M(T)$ curves, the monoaxial $\text{Cr}_{1/3}\text{NbS}_2$ exhibits strong anisotropic magnetization, which should be investigated by the angle dependent of magnetization $[M(\varphi)]$. Figure 3 shows the out-of-plane and in-plane $M(\varphi)$ at selected temperature. The in-plane $M(\varphi)$ was measured under the field within the ab -plane, while the out-of-plane one was performed under the field rotated from c -axis to ab -plane. It can be seen that the in-plane $M(\varphi)$ display isotropic magnetization. However, out-of-plane $M(\varphi)$ at 2 K and 100 K exhibits a shape of butterfly, which suggests strong magnetic anisotropy. The magnetization in ab -plane is much stronger than that along c -axis, suggesting that the spins are ordered

within the ab -plane. The out-of-plane $M(\varphi)$ at 150 K exhibits slightly magnetic anisotropy, which is much weaker than those at 100 K or 2 K. The slight magnetic anisotropy at 150 K may be attributed to the precursor or fluctuation phenomenon analogy to that in FeGe²⁹. The out-of-plane $M(\varphi)$ at 300 K does not display any magnetic anisotropy.

Figure 4 (a) and (b) plot the isothermal magnetization [$M(H)$] at selected temperature with $H \perp c$ and $H//c$, respectively. The magnified $M(H)$ curves in low field region are depicted in Fig. 4 (c) and (d). When $H \perp c$, M becomes saturated rapidly with very small saturation field ($H_S \sim 0.7$ kOe), as shown in Fig. 4 (c). When $H//c$, M becomes saturated slowly with large saturation field ($H_S \sim 25$ kOe), as given in Fig. 4 (b). However, the same saturation magnetization (M_S) is attained regardless of the direction of applied field. For $M(H)$ with $H \perp c$ at 2 K and 100 K below T_C , it exhibits two symmetrical magnetic steps in low field region before saturation. Moreover, a loop is found at the magnetic step between increase and decrease of field, which has been also found in previous works³⁰. However, when $H//c$, no step or loop is found on the $M(H)$ curves. To better understand the $M(H)$ loops, the $M(H)$ with $H \perp c$ was measured at different temperatures, as shown in Fig 5 (a). The curves in Fig 5 (a) are elevated vertically for clear clarity. As can be seen, the loop becomes smaller as the temperature increases. The width of the $M(H)$ loop (ΔH) as a function of temperature is extracted to plot in Fig. 5 (b), which displays that the ΔH decreases with the increase of temperature. The loop disappears when temperature exceeds 120 K. It is well known that Cr_{1/3}NbS₂ undergoes a field-induced transition from HM to CSL below T_C . Moreover, the CSL state is polarized to FFM, accompanied with a transition from incommensurate to commensurate states. In fact, this kind of $M(H)$ loop is usually found in the magnetic metastable transition system, such as UP_{0.9}S_{0.1} and EuSe³¹. The $M(H)$ loop originates during the formation and collapse of the magnetic metastate by the applied field³¹. The $M(H)$ loops in Cr_{1/3}NbS₂ assemble those observed in the ferrimagnetic or antiferromagnetic metastable, where $M(H)$ loop occurs between phase transitions induced by the field. Therefore, $M(H)$ loops in Cr_{1/3}NbS₂ confirms that the CSL state is a magnetic metastable³¹.

In order to uncover the magnetic coupling in Cr_{1/3}NbS₂, the critical behavior is investigated. Figure 6 (a) gives the initial isothermal $M(H)$ around T_C with $H \perp c$, and the Arrott plot of M^2 vs. H/M is depicted in Fig. 6 (b). All curves on the Arrott plot display non-linear behaviors even in the high field region, which suggests that the magnetic interaction

in $\text{Cr}_{1/3}\text{NbS}_2$ cannot be described by the conventional Landau mean-field model^{32,33}. The order of the phase transition can be determined by the slope from the Arrott plot according to the Banerjee's criterion, where a negative slope suggests a first-order transition and a positive slope implies a second-order one³⁴. The positive slopes of M^2 vs. H/M curves reveal that the phase transition in $\text{Cr}_{1/3}\text{NbS}_2$ is of a second order.

In the vicinity of a second order magnetic phase transition, the spontaneous magnetization M_S and initial susceptibility χ_0 can be described by a series of functions^{35,36}:

$$M_S(T) = M_0(-\varepsilon)^\beta, \varepsilon < 0, T < T_C \quad (1)$$

$$\chi_0^{-1}(T) = (h_0/M_0)\varepsilon^\gamma, \varepsilon > 0, T > T_C \quad (2)$$

$$M = DH^{1/\delta}, \varepsilon = 0, T = T_C \quad (3)$$

where $\varepsilon = (T - T_C)/T_C$ is the reduced temperature; M_0/h_0 and D are critical amplitudes. The parameters β (associated with M_S), γ (associated with χ_0), and δ (associated with T_C) are the critical exponents. The critical behavior around the critical temperature can be described by a series of critical exponents, which follow the Arrott-Noakes equation of state in asymptotic critical region³⁷:

$$(H/M)^{1/\gamma} = (T - T_C)/T_C + (M/M_1)^{1/\beta} \quad (4)$$

where M_1 is a constant. The critical exponents implies significant clues of magnetic interactions, such as the correlating length, spin-dimensionality, and decaying distance of magnetic coupling. Four series of critical exponents belonging to the 3D-Heisenberg model ($\beta = 0.365$, $\gamma = 1.386$), 3D-Ising model ($\beta = 0.325$, $\gamma = 1.24$), 3D-XY model ($\beta = 0.345$, $\gamma = 1.316$), and tricritical mean-field model ($\beta = 0.25$, $\gamma = 1.0$) are tried to construct the modified Arrott plots^{33,38}, as shown in Figs. 7 (a), (b), (c), and (d) respectively. All the curves in these four constructions exhibit quasi-straight lines in high field region. However, the lines in Fig. 7 (d) are not parallel to each other, indicating that the tricritical mean-field is dissatisfied. However, for Figs. 7 (a), (b) and (c), it is difficult to distinguish which model is the best. As we know, for an ideal model, the modified Arrott plot should display a series of parallel lines in high field region with the same slope which defined as $S(T) = dM^{1/\beta}/d(H/M)^{1/\gamma}$. Thus, in an ideal model, the slopes of $M^{1/\beta}$ vs. $(H/M)^{1/\gamma}$ lines should exhibit the sample value as that at T_C . We define the normalized slope (NS) as $NS = S(T)/S(T_C)$. For a most

satisfied model, all NS values should approach '1' closely. By this method, it enables us to distinguish the most suitable model by comparing the NS with the ideal value of '1'^{39–41}. Plot of NS vs. T for the four different models is shown in Fig. 8. It can be seen that the NS of 3D-Heisenberg model is close to '1' mostly among these models.

More accurate critical exponents β and γ can be obtained by the iteration method⁴², which are used to distinguish which universality class they belong to. The initial parameters are based on those of Fig. 7 (a) since its NS values are close to '1' mostly. The linear extrapolation from high field region to the intercepts with the axes $M^{1/\beta}$ and $(H/M)^{1/\gamma}$ yields $M_S(T, 0)$ and $\chi_0^{-1}(T, 0)$ under zero field. By fitting to Eqs. (1) and (2), a set of β and γ is obtained, which is used to reconstruct a new modified Arrott plot. Subsequently, new $M_S(T, 0)$ and $\chi_0^{-1}(T, 0)$ are generated from the linear extrapolation from high field region. By this way, another set of β and γ can be obtained. This procedure is repeated until β and γ hardly change. **The final obtained critical exponents by the iteration method are independent on the initial parameters.** In this way, $\beta = 0.370(4)$ with $T_C = 126.4(7)$ and $\gamma = 1.380(2)$ with $T_C = 126.1(1)$ are obtained for $\text{Cr}_{1/3}\text{NbS}_2$, as shown in Fig 9 (a). The obtained T_C is consistent with that obtained by T. Miyadai *et al*¹³. Figure 9 (b) shows the initial $M(H)$ at the critical temperature $T_C = 126$ K, with the inset plotted on a log – log scale. One can see that the $M(H)$ at T_C exhibits a straight line on a log – log scale when $H > H_S$. Thus, $\delta = 4.853(6)$ is determined in the high field region ($H > H_S$) based on Eq. (3). According to the statistical theory, these critical exponents should fulfill the Widom scaling law⁴³:

$$\delta = 1 + \frac{\gamma}{\beta} \quad (5)$$

According to the Widom scaling law $\delta = 4.729(7)$ is calculated, which is in agreement with that obtained from the experimental critical isothermal analysis. The self-consistency of the critical exponents demonstrates that they are reliable and unambiguous.

The final critical exponents ($\beta = 0.370(4)$, $\gamma = 1.380(2)$, $\delta = 4.853(6)$) are in agreement with those recently reported by E. Clements *et al.*,⁴⁴ which confirm the reliability of these obtained exponents. Both sets of exponents from these two works are very close to the theoretical prediction of 3D-Heisenberg model ($\beta = 0.365$, $\gamma = 1.386$, $\delta = 4.80$), which suggest a short-rang magnetic coupling of Cr-Cr^{33,44}. Although the structure of $\text{Cr}_{1/3}\text{NbS}_2$ is two-dimensional, its magnetic coupling is of a three-dimensional type. This indicates that the magnetic interactions of Cr-Cr are coupled not only within the ab -plane but also

between the inter-layers along the c -axis. As we know, the DM interaction plays an important role in the magnetic structure of $\text{Cr}_{1/3}\text{NbS}_2$, which makes the spins exhibit spiral ordering. However, the DM interaction has rarely effect on the critical exponents due to two aspects. The DM interaction is much weaker than the ferromagnetic exchange, which is only $1 \sim 2$ orders of magnitude of the ferromagnetic exchange⁴⁵. Thus, the critical exponents are mainly determined by the magnetic exchange interaction. In fact, in the systems with DM interaction such as FeGe , MnSi , Cu_2OSeO_3 , $\text{Fe}_{0.8}\text{Co}_{0.2}\text{Si}$, their critical exponents are either rarely influenced by the DM interaction^{42,45–47}.

For a homogeneous magnet, M. E. Fisher *et al.* theoretically treated the magnetic ordering as attractive interaction of spins, where a renormalization group theory analysis suggests the exchange distance $J(r)$ decays with distance r as^{48,49}:

$$J(r) \approx r^{-(d+\sigma)} \quad (6)$$

where d is spatial-dimensionality, and σ is a critical exponent which can calculated as^{49,50}:

$$\gamma = 1 + \frac{4n+2}{dn+8}\Delta\sigma + \frac{8(n+2)(n-4)}{d^2(n+8)^2} \left[1 + \frac{2G(\frac{d}{2})(7n+20)}{(n-4)(n+8)} \right] \Delta\sigma^2 \quad (7)$$

where $\Delta\sigma = (\sigma - \frac{d}{2})$, $G(\frac{d}{2}) = 3 - \frac{1}{4}(\frac{d}{2})^2$, n is the spin-dimensionality. For the 3D-Heisenberg model, there is $d = 3$ and $n = 3$. It can be obtained that $\sigma = 1.932(6)$ for $\text{Cr}_{1/3}\text{NbS}_2$, which indicates that the magnetic interaction decays on spatial distance as $J(r) \sim r^{-4.942,49}$. It has been suggested that if $J(r)$ decreases with distance r faster than r^{-5} , the Heisenberg exponents are valid for a three-dimensional isotropic ferromagnet⁴⁹. As we know, these critical exponents should follow the scaling equations. Defining the renormalized magnetization $m \equiv \varepsilon^{-\beta}M(H, \varepsilon)$ and the renormalized field $h \equiv H\varepsilon^{-(\beta+\gamma)}$, in the asymptotic critical region the scaling equations can be written as³⁵:

$$m = f_{\pm}(h) \quad (8)$$

where f_{\pm} are regular functions denoted as f_+ for $T > T_C$ and f_- for $T < T_C$. The scaling equations indicate that m vs. h should form two universal branches for $T > T_C$ and $T < T_C$ respectively, even those in low field region^{51,52}. However, if a field-induced phase transition occurs, the scaling becomes divergent at the boundary between the phases. The divergence of the scaling curves supplies a method to distinguish the different phases⁴². Based on the scaling equation, the isothermal magnetization around the critical temperatures for

$\text{Cr}_{1/3}\text{NbS}_2$ are replotted in Fig. 10 (a), and the typical m vs. h curves are shown on log-log scale in the Fig. 10 (b) to magnify those in low field region. It can be seen that experimental data collapse into two universal curves, except the $M - T - H$ in the low field region. Especially, the m vs. h on log-log scale is depicted in Fig. 10 (c), where the magnetic transitions in low field region are displayed. Furthermore, m^2 vs. h/m curves clearly distinguish the different phases in low field region, as shown in Fig. 10 (d). Three regions separated by two transitions are clearly seen on m^2 vs. h/m curves, which are corresponding to the HM, CSL, and FFM states. In very low field region, a platform is found on m^2 vs. h/m curves, which is corresponding to the HM state. With the increase of field, the abrupt increase region of m^2 vs. h/m is attributed to the CSL transition, where the critical field from HM to CSL is defined as H_1 . When H exceeds H_S (H_S is the critical field from CSL to FFM), the CSL is completely polarized into FFM state. In the CSL region, the state can be further identified by the slope (S) of m^2 vs. h/m . In fact, the transition from CSL to FFM phase is a procedure of competition between CSL and FFM. In lower field region, the CSL is dominant where the magnetic solitons are separated by the FM region (CSL-1 state)¹⁵. In higher field region, the FFM phase becomes dominant in the system, where the whole magnetization is very close to the FM behavior (CSL-2 state)¹⁵. It can be seen that the change from negative to positive occurs to S of m^2 vs. h/m in the CSL region, where the critical field from CSL-1 to CSL-2 is defined as H_2 . As we know, the FFM behavior exhibits positive S ($S > 0$)³⁴. Thus, the positive S in CSL region corresponds to CSL-2 (with large FM array) which approaches the FFM behavior with $S > 0$. Alternatively, the region of $S < 0$ is corresponding to CSL-1 (dominant helical texture with poor FM array)¹⁵. By this method, we can distinguish the CSL-1 from CSL-2 states.

Based on the scaling of the $M - T - H$, the $H - T$ phase diagram with $H \perp c$ is constructed in Fig. 11. Since the critical scaling is restrict within the critical temperature region ($|(T - T_C)/T_C| \leq 0.1$), only the phase diagram around T_C is mapped. It can be seen that $\text{Cr}_{1/3}\text{NbS}_2$ exhibits a HM ground state below $T_C \sim 127$ K. When field is applied, the HM state is modulated to CSL-1, and subsequently changes to CSL-2 state. Finally, the CSL-2 state is polarized into FFM phase when H exceeds H_C . Two critical points can be determined on the $H - T$ phase diagram, as shown in Fig. 11. In fact, in the monoaxial chiral helimagnetic system, two tricritical points have been predicted theoretically by V. Laliena

et al. when the field is applied along variable directions²⁷. However, in another work, they suggests a tricritical point and a zero-field critical one in monoaxial helimagnet when field is applied along the c -axis²⁴. The zero-field critical point locates at boundary from HM to PM phases²⁴. Therefore, in present case, one critical point corresponds to a tricritical one, which locates at the intersection between the CSL, FFM, and PM phases (~ 310 Oe at 127 K). The other one is determined as zero-field critical point, which is situated at the boundaries between HM, CSL and PM phases (~ 85 Oe at 127 K).

IV. CONCLUSION

In summary, the magnetism of the single crystal $\text{Cr}_{1/3}\text{NbS}_2$ is investigated. The magnetization displays strong magnetic anisotropy when the external field is applied parallel and perpendicularly to the c -axis ($H < H_S$). The $M(H)$ curve with $H \perp c$ displays a loop on the boundary of the phase transition from incommensurate CSL to commensurate FFM, which suggests that the CSL phase is a magnetic metastable. The critical exponents of $\text{Cr}_{1/3}\text{NbS}_2$ are obtained as $\beta = 0.370(4)$, $\gamma = 1.380(2)$, and $\delta = 4.853(6)$, which are close to the theoretical prediction of 3D-Heisenberg model. The critical behavior indicates the magnetic coupling is of a short-range type. Based on the scaling equation, the $H - T$ phase diagram around T_C is constructed, where two critical points are determined. One critical point is a tricritical one, which locates at the intersection between the CSL, FFM, and PM states. The other critical point is a zero-field critical one, which is situated at the intersection between CSL, HM and PM states.

V. ACKNOWLEDGEMENTS

This work is supported by the National Key R&D Program of China (Grant No. 2017YFA0303201) and the National Natural Science Foundation of China (Grant Nos. 11574322, U1732276, 11474290, and 11574288). D. S. and D. G. M. acknowledge support from the National Science Foundation under grant DMR-1410428.

* Corresponding author. Email:zhanglei@hmfl.ac.cn

- [†] Corresponding author. Email: dmandrus@utk.edu
- ¹ U. K. Rößler, A. N. Bogdanov, and C. Pfleiderer, *Nature (London)* **442**, 797 (2006).
- ² S. Mühlbauer, B. Binz, F. Jonietz, C. Pfleiderer, A. Rosch, A. Neubauer, R. Georgii, and P. Böni, *Science* **323**, 915 (2009).
- ³ X. Yu, Y. Onose, N. Kanazawa, J. Park, J. Han, Y. Matsui, N. Nagaosa, and Y. Tokura, *Nature (London)* **465**, 901 (2010).
- ⁴ S. Seki, X. Z. Yu, S. Ishiwata, and Y. Tokura, *Science*, **336**, 198 (2012).
- ⁵ F. N. Rybakov, A. B. Borisov, S. Blügel, and N. S. Kiselev, *Phys. Rev. Lett.* **115**, 117201 (2015).
- ⁶ I. Dzyaloshinsky, *J. Phys. Chem. Solids* **4**, 241 (1958).
- ⁷ T. Moriya, *Phys. Rev.* **120**, 91 (1960).
- ⁸ A. Bauer and C. Pfleiderer, *Phys. Rev. B* **85**, 214418 (2012).
- ⁹ Y. Togawa, Y. Kousaka, S. Nishihara, K. Inoue, J. Akimitsu, A. S. Ovchinnikov, and J. Kishine, *Phys. Rev. Lett.* **111**, 197204 (2013).
- ¹⁰ Y. Togawa, T. Koyama, K. Takayanagi, S. Mori, Y. Kousaka, J. Akimitsu, S. Nishihara, K. Inoue, A. S. Ovchinnikov, and J. Kishine, *Phys. Rev. Lett.* **108**, 107202 (2012).
- ¹¹ Y. Masaki and R. L. Stamps, *Phys. Rev. B* **95**, 024418 (2017).
- ¹² N. J. Ghimire, M. A. McGuire, D. S. Parker, B. Sipos, S. Tang, J. Q. Yan, B. C. Sales, and D. Mandrus, *Phys. Rev. B* **87**, 104403 (2013).
- ¹³ T. Miyadai, K. Kikuchi, H. Kondo, S. Sakka, K. Arai, and Y. Ishikawa, *J. Phys. Soc. Jpn.* **52**, 1394 (1983).
- ¹⁴ F. Hulliger and E. Pobitschka, *J. Solid State Chem.* **1**, 117 (1970).
- ¹⁵ K. Tsuruta, M. Mito, H. Deguchi, J. Kishine, Y. Kousaka, J. Akimitsu, and K. Inoue, *Phys. Rev. B* **93**, 104402 (2016).
- ¹⁶ J. Kishine, A. S. Ovchinnikov, and I. V. Proskurin, *Phys. Rev. B* **82**, 064407 (2010).
- ¹⁷ A. B. Borisov, J. Kishine, I. G. Bostrem, and A. S. Ovchinnikov, *Phys. Rev. B* **79**, 134436 (2009).
- ¹⁸ K. Koumpouras, A. Bergman, O. Eriksson, and D. Yudin, *Sci. Rep.* **6**, 25685 (2016).
- ¹⁹ S. Mankovsky, S. Polesya, H. Ebert, and W. Bensch, *Phys. Rev. B* **94**, 184430 (2016).
- ²⁰ N. Sirica, S. K. Mo, F. Bondino, I. Pis, S. Nappini, P. Vilmercati, J. Yi, Z. Gai, P. C. Snijders, P. K. Das, I. Vobornik, N. Ghimire, M. R. Koehler, L. Li, Sapkota, D. S. Parker, D. G. Mandrus,

- and N. Mannella, Phys. Rev. B **94**, 075141 (2016).
- ²¹ Y. Togawa, Yusuke Kousaka, Katsuya Inoue, and J. Kishine, J. Phys. Soc. Jpn. **85**, 112001 (2016).
- ²² Y. Togawa, T. Koyama, Y. Nishimori, Y. Matsumoto, S. McVitie, D. McGrouther, R. L. Stamps, Y. Kousaka, J. Akimitsu, S. Nishihara, K. Inoue, I. G. Bostrem, Vl. E. Sinitsyn, A. S. Ovchinnikov, and J. Kishine, Phys. Rev. B **92**, 220412(R) (2015).
- ²³ B. J. Chapman, A. C. Bornstein, N. J. Ghimire, D. Mandrus, and M. Lee, Appl. Phys. Lett. **105**, 072405 (2014).
- ²⁴ V. Laliena, J. Campo, and Y. Kousaka, Phys. Rev. B **94**, 094439 (2016).
- ²⁵ Y. Nishikawa and K. Hukushima, Phys. Rev. B **94**, 064428 (2016).
- ²⁶ M. Shinozaki, S. Hoshino, Y. Masaki, J. Kishine, and Y. Kato, J. Phys. Soc. Jpn. **85**, 074710 (2016).
- ²⁷ V. Laliena, J. Campo, J. Kishine, A. S. Ovchinnikov, Y. Togawa, Y. Kousaka, and K. Inoue, Phys. Rev. B **93**, 134424 (2016).
- ²⁸ V. Dyadkin, F. Mushenok, A. Bosak, D. Menzel, S. Grigoriev, P. Pattison, and D. Chernyshov, Phys. Rev. B **91**, 184205 (2015).
- ²⁹ H. Wilhelm, M. Baenitz, M. Schmidt, U. K. Rößler, A. A. Leonov, and A. N. Bogdanov, Phys. Rev. Lett. **107**, 127203 (2011).
- ³⁰ K. Tsuruta, M. Mito, Y. Kousaka, J. Akimitsu, J. Kishine, Y. Togawa, H. Ohsumi, and K. Inoue, J. Phys. Soc. Jpn **85**, 013707 (2016).
- ³¹ E. Stryjewski and N. Giordano, Adv. Phys. **26**, 487 (1977).
- ³² A. Arrott, Phys. Rev. **108**, 1394 (1957).
- ³³ S. N. Kaul, J. Magn. Magn. Mater. **53**, 5 (1985).
- ³⁴ B. K. Banerjee, Phys. Lett. **12**, 16 (1964).
- ³⁵ H. E. Stanley, *Introduction to Phase Transitions and Critical Phenomena* (Oxford University Press, London, 1971).
- ³⁶ M. E. Fisher, Rev. Mod. Phys. **46**, 597 (1974).
- ³⁷ A. Arrott and J. Noakes, Phys. Rev. Lett. **19**, 786 (1967).
- ³⁸ K. Huang, *Statistical Mechanics*, 2nd ed. (Wiley, New York, 1987).
- ³⁹ L. Zhang, B. S. Wang, Y. P. Sun, P. Tong, J. Y. Fan, C. J. Zhang, L. Pi, and Y. H. Zhang, Phys. Rev. B **85**, 104419 (2012).

- ⁴⁰ J. Y. Fan, L. S. Ling, B. Hong, L. Zhang, L. Pi, and Y. H. Zhang, *Phys. Rev. B* **81**, 144426 (2010).
- ⁴¹ L. Zhang, J. Y. Fan, L. Li, R. W. Li, L. S. Ling, Z. Qu, W. Tong, S. Tan, and Y. H. Zhang, *Europhys. Lett.* **91**, 57001 (2010).
- ⁴² L. Zhang, D. Menzel, C. M. Jin, H. F. Du, M. Ge, C. J. Zhang, L. Pi, M. L. Tian, and Y. H. Zhang, *Phys. Rev. B* **91**, 024403 (2015).
- ⁴³ L. P. Kadanoff, *Physics* **2**, 263 (1966).
- ⁴⁴ E. M. Clements, R. Das, L. Li, P. J. Lampen-Kelley, M. H. Phan, V. Keppens, D. Mandrus, and H. Srikanth, *Sci. Rep.* **7**, 6545 (2017).
- ⁴⁵ H. Wilhelm, A. O. Leonov, U. K. Rößler, P. Burger, F. Hardy, C. Meingast, M. E. Gruner, W. Schnelle, M. Schmidt, and M. Baenitz, *Phys. Rev. B* **94**, 144424 (2016).
- ⁴⁶ I. Živković, J. S. White, H. M. Rønnow, K. Prša, and H. Berger, *Phys. Rev. B* **89**, 060401(R) (2014).
- ⁴⁷ W. J. Jiang, X. Z. Zhou, and G. Williams, *Phys. Rev. B* **82**, 144424 (2010).
- ⁴⁸ K. Ghosh, C. J. Lobb, R. L. Greene, S. G. Karabashev, D. A. Shulyatev, A. A. Arsenov, Y. Mukovskii, *Phys. Rev. Lett.* **81**, 4740 (1998).
- ⁴⁹ M. E. Fisher, S. K. Ma, and B. G. Nickel, *Phys. Rev. Lett.* **29**, 917 (1972).
- ⁵⁰ S. F. Fischer, S. N. Kaul, H. Kronmüller, *Phys. Rev. B* **65**, 064443 (2002).
- ⁵¹ M. H. Phan, V. Franco, N. Bingham, H. Srikanth, N. Hur, and S. Yu, *J. Alloys Compd.* **508**, 238 (2010).
- ⁵² N. Khan, A. Midya, K. Mydeen, P. Mandal, A. Loidl, and D. Prabhakaran, *Phys. Rev. B* **82**, 064422 (2010).

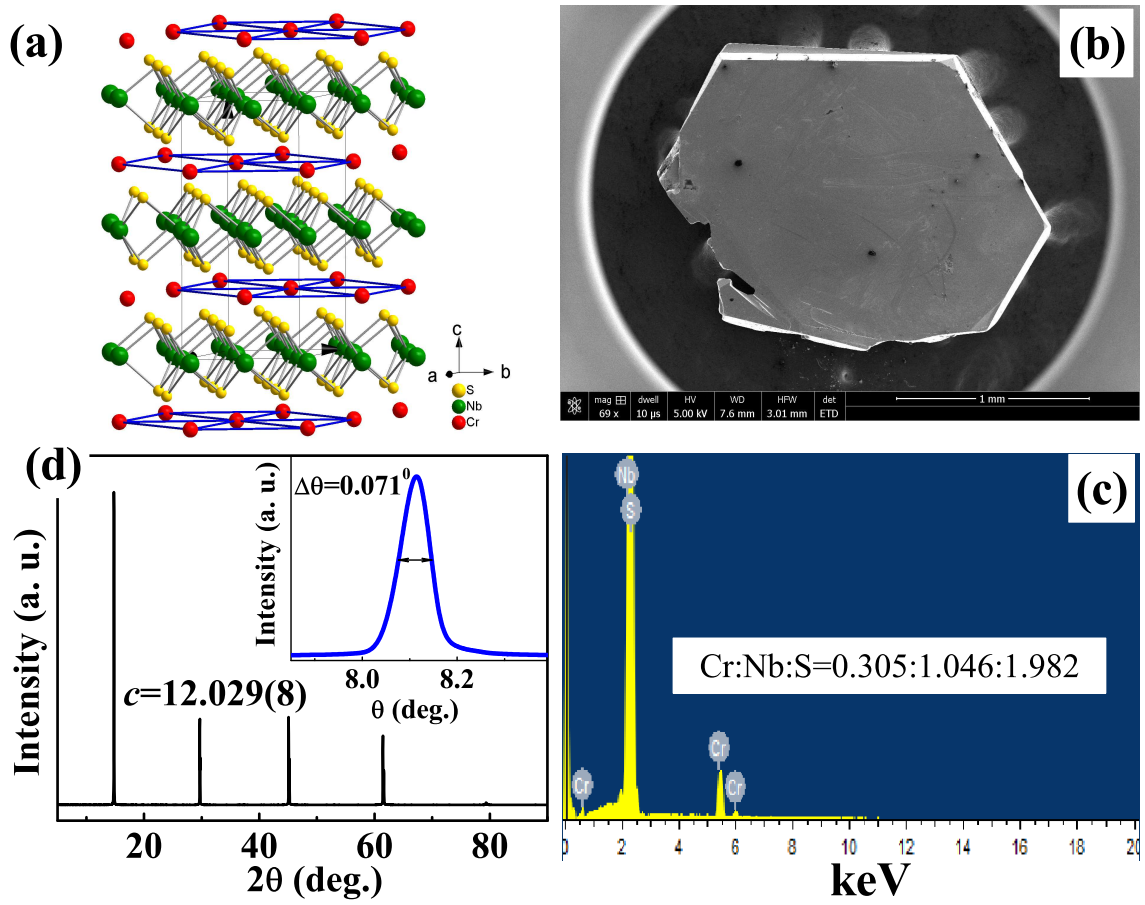


FIG. 1: (Color online) (a) The crystal structure of $\text{Cr}_{1/3}\text{NbS}_2$; (b) the morphology of $\text{Cr}_{1/3}\text{NbS}_2$ single crystal; (c) a typical EDX spectrum for single crystal $\text{Cr}_{1/3}\text{NbS}_2$; (d) XRD pattern of the plane (the inset shows the rock curve).

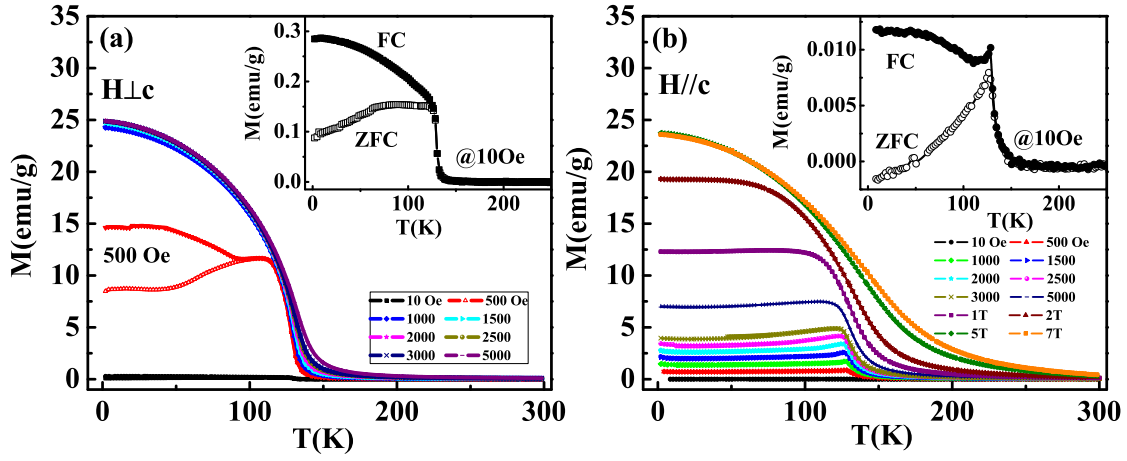


FIG. 2: (Color online) Temperature dependence of magnetization [$M(T)$] under selected fields for $\text{Cr}_{1/3}\text{NbS}_2$ with (a) $H \perp c$ and (b) $H // c$ (the insets show the ZFC and FC curves under 10 Oe with $H \perp c$ and $H // c$ respectively).

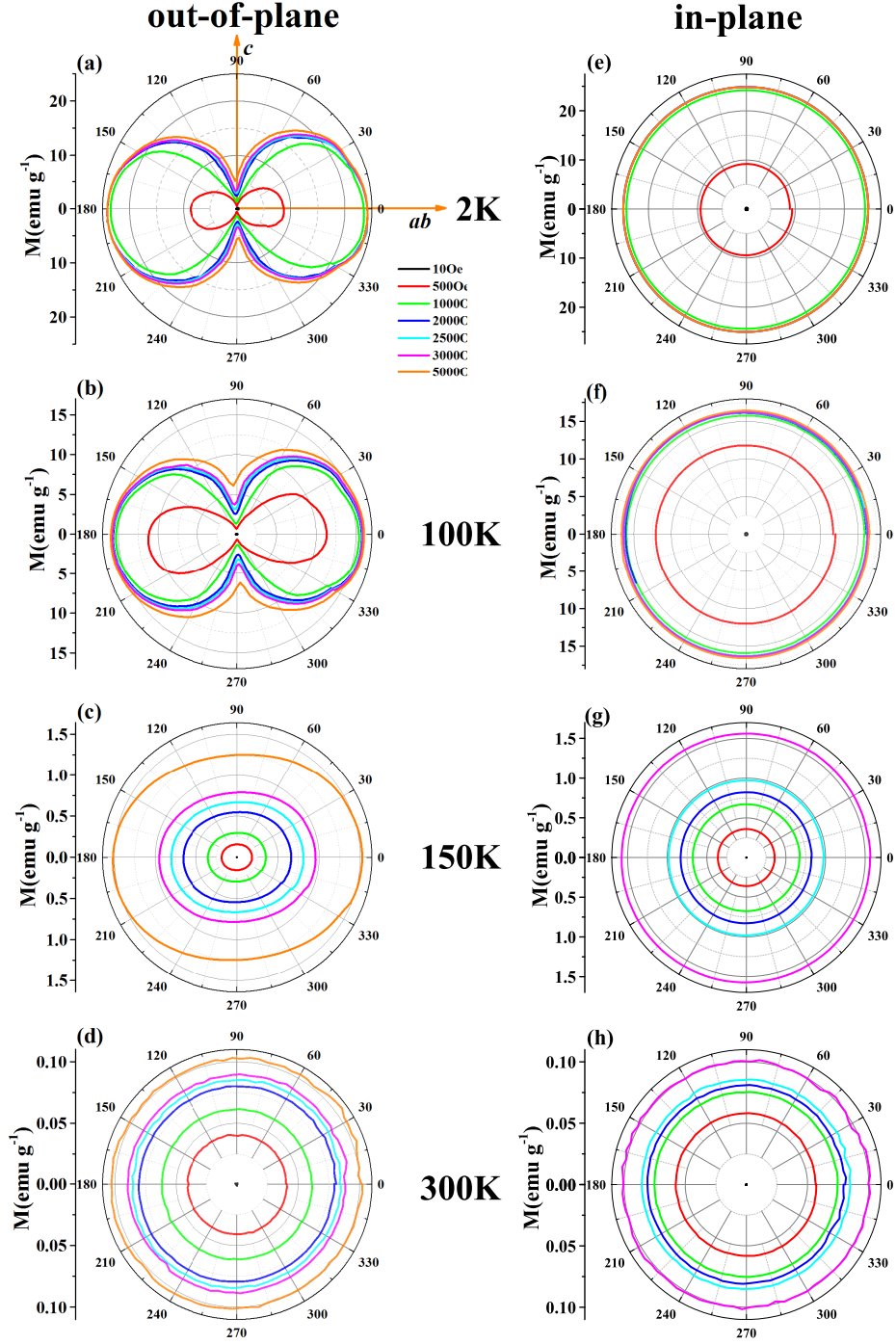


FIG. 3: (Color online) (a) The out-of-plane and in-plane magnetization as a function of rotation angle $[M(\varphi)]$ at selected temperature for $\text{Cr}_{1/3}\text{NbS}_2$ (the curves under different fields are distinguished by different colors).

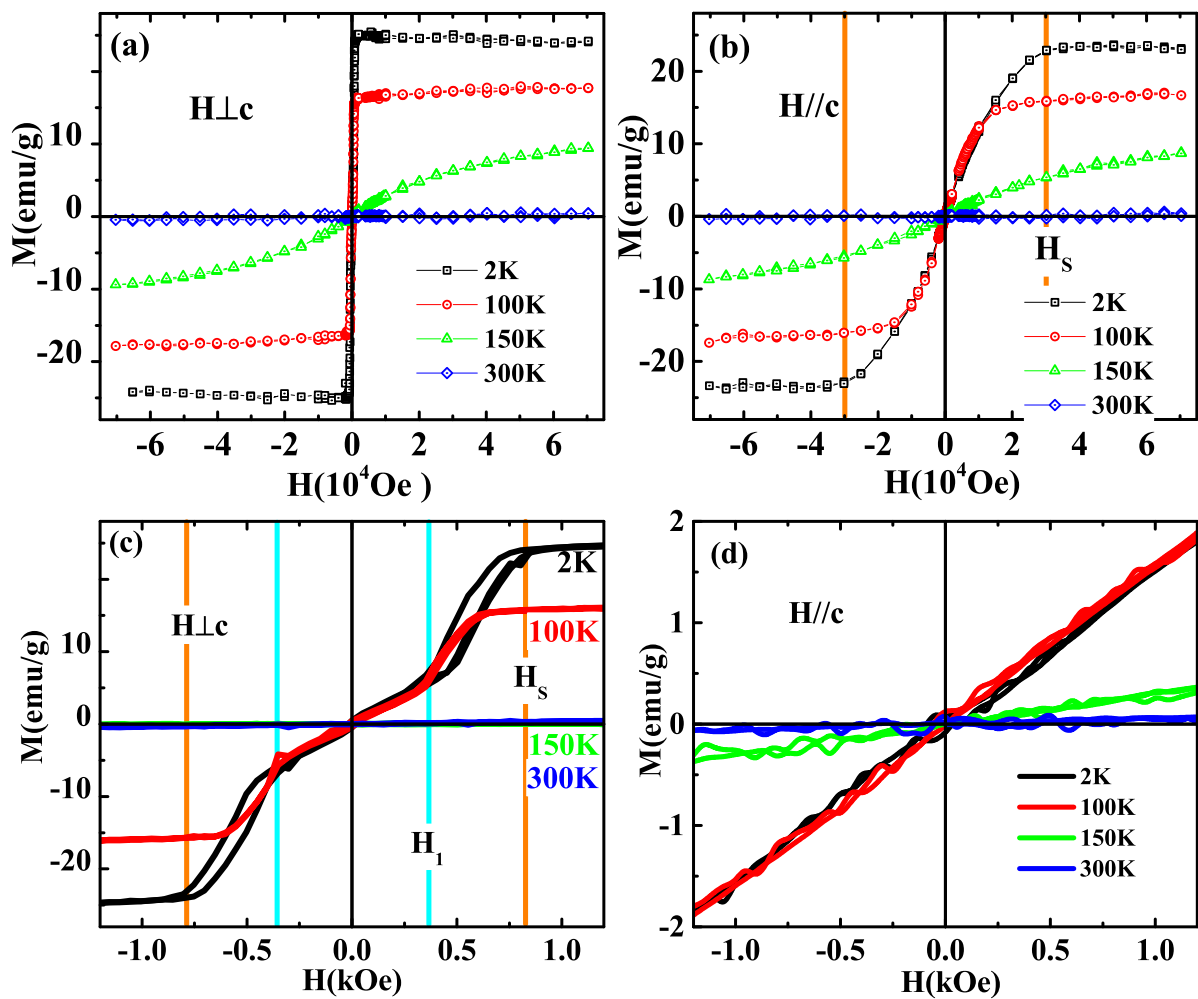


FIG. 4: (Color online) (a) and (b) Isothermal magnetization as a function of field [$M(H)$] at selected temperature with $H \perp c$ and $H // c$; (c) and (d) the magnified $M(H)$ in low field region.

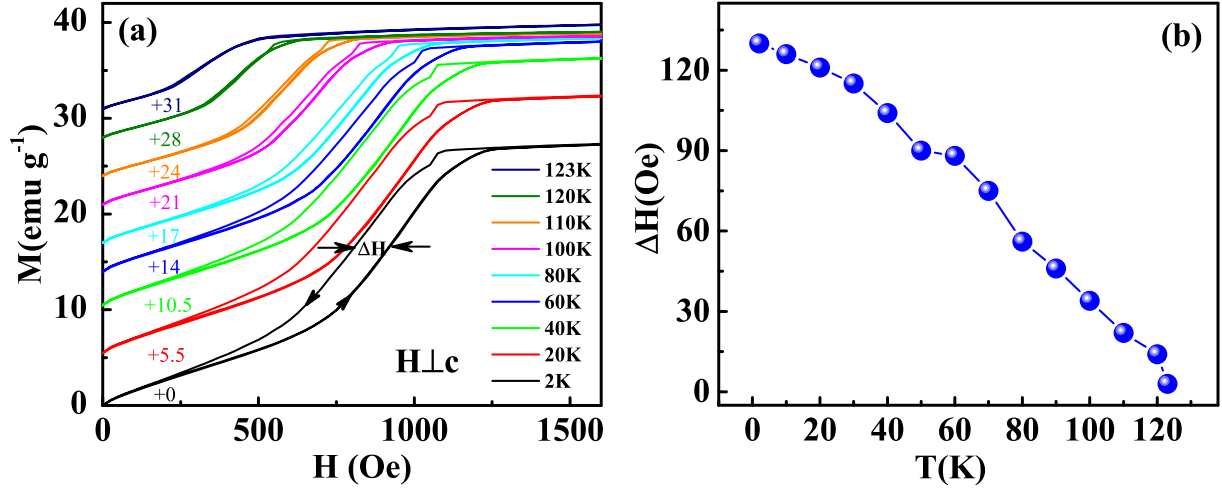


FIG. 5: (Color online) (a) The $M(H)$ loops with $H \perp c$ (the curves are elevated vertically for clarity, and the elevation values are marked); (b) the width of the $M(H)$ loop (ΔH) as a function of temperature.

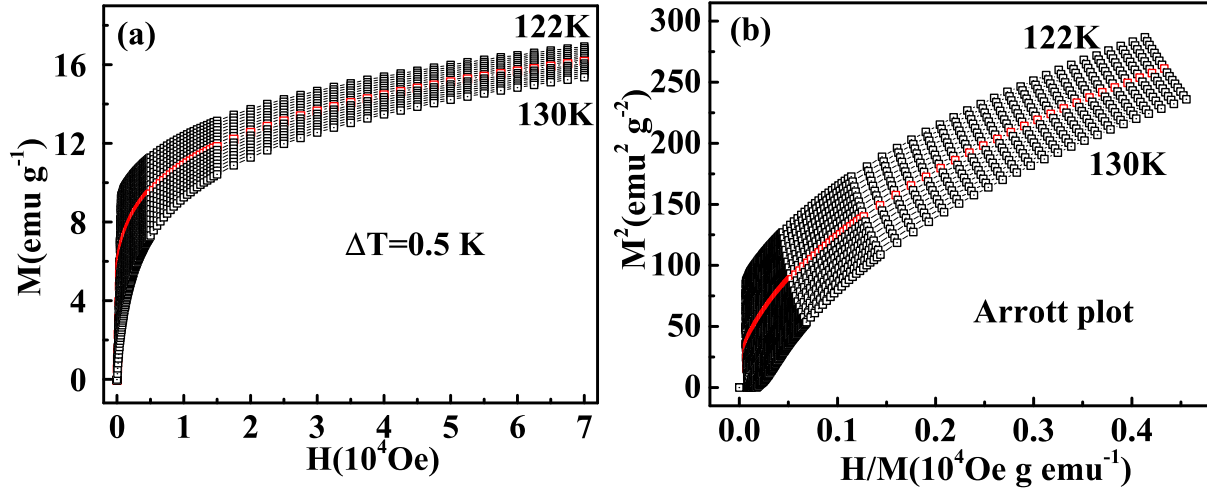


FIG. 6: (Color online) (a) The initial isothermal $M(H)$ around T_C with $H \perp c$; (b) the Arrott plot for $\text{Cr}_{1/3}\text{NbS}_2$ (the curves at T_C are marked in red color).

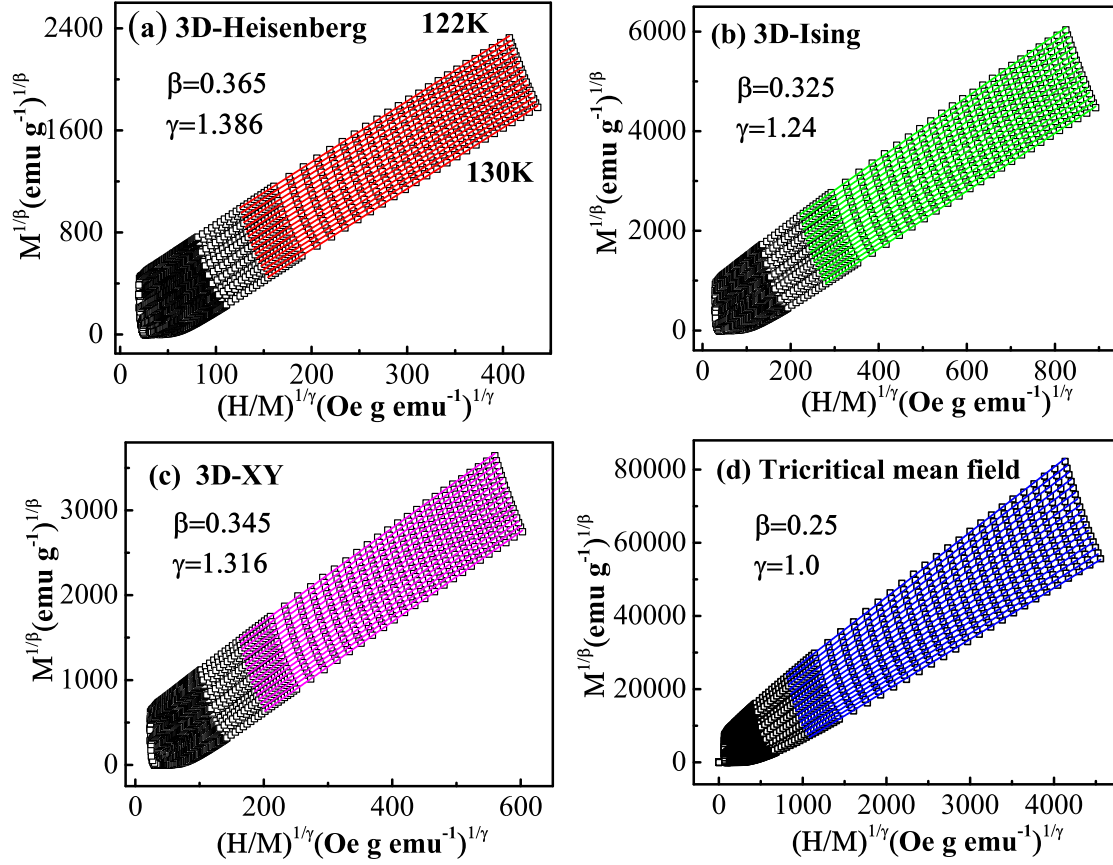


FIG. 7: (Color online) The isotherms of $M^{1/\beta}$ vs. $(H/M)^{1/\gamma}$ fitted by lines with parameters of (a) 3D-Heisenberg model (red), (b) 3D-Ising model (green), (c) 3D-XY model (magenta), and (d) tricritical mean-field model (blue).

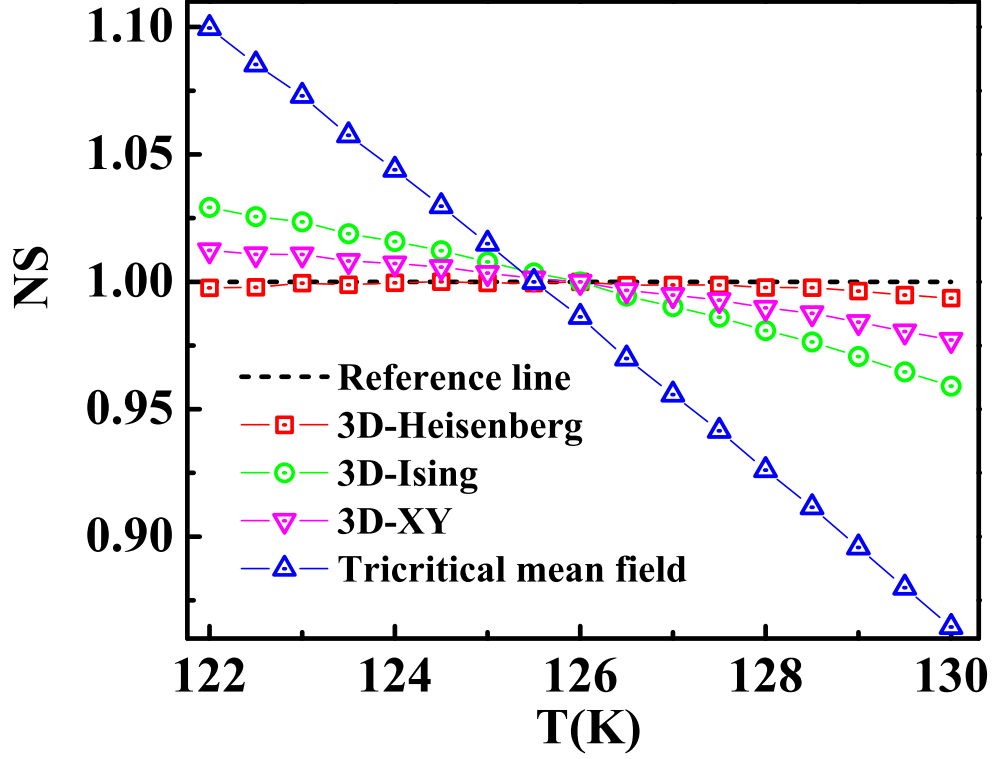


FIG. 8: (Color online) Temperature dependence of normalized slope (NS) for the four theoretical models.

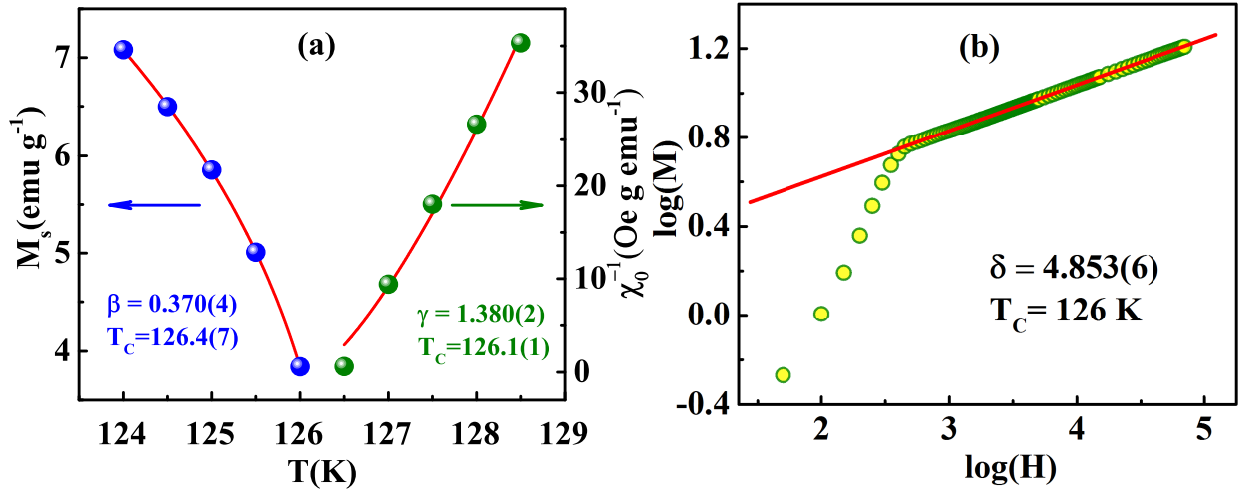


FIG. 9: (Color online) (a) The M_S (left) and χ_0^{-1} (right) as a function of temperature for $\text{Cr}_{1/3}\text{NbS}_2$; (b) isothermal $M(H)$ at T_C on log-log scale (red solid curves and line are fitted).

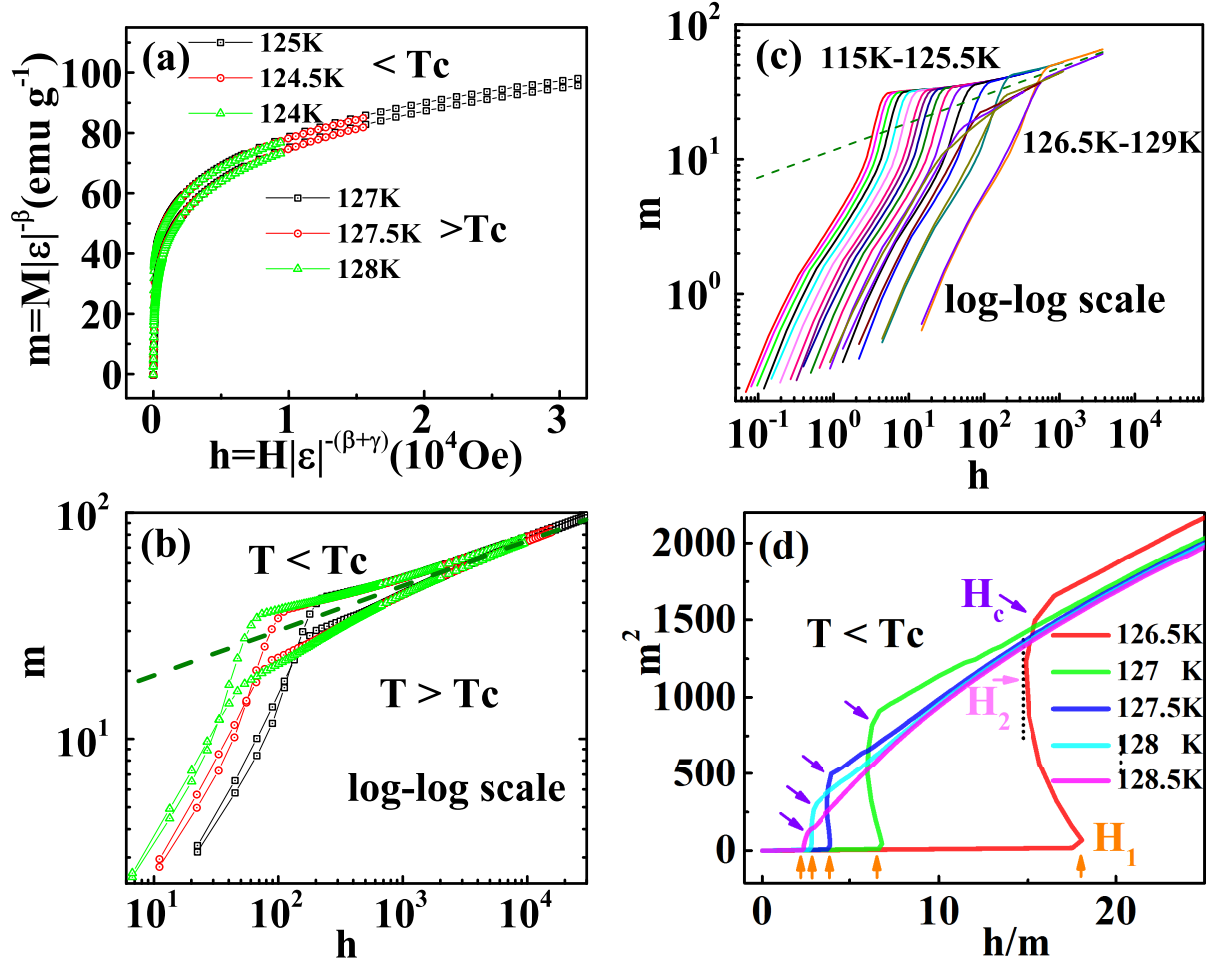


FIG. 10: (Color online) (a) Scaling plot of m vs. h around T_C for $M - H$ at typical temperature; (b) typical m vs. h curves on log-log scale; (c) the magnification of m vs. h in low field region; (d) the re-scaling of m^2 vs. h/m (H_1 is the critical field from HM to CSL-1; H_2 is the critical field from CSL-1 to CSL-2; and H_C is the critical field from CSL-2 to FFM).

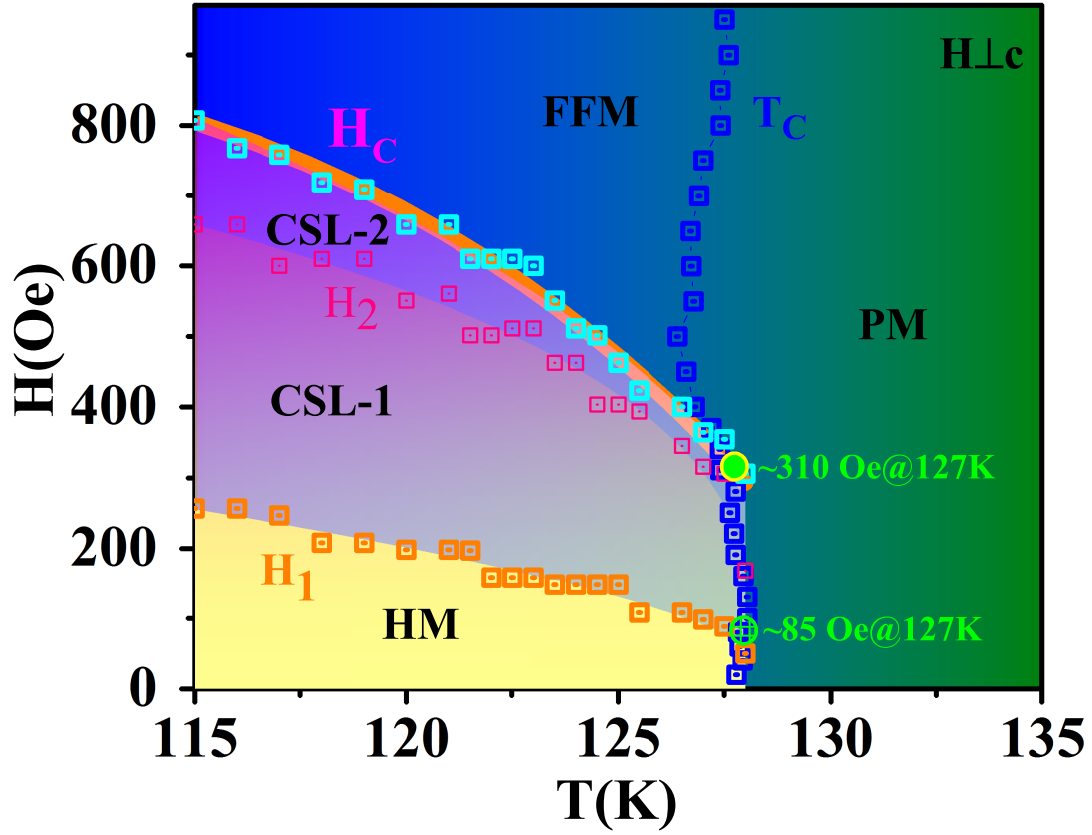


FIG. 11: (Color online) The $H - T$ phase diagram in the vicinity of the phase transition obtained by scaling of the $M - T - H$ for $\text{Cr}_{1/3}\text{NbS}_2$ with $H \perp c$ (HM corresponds to the helimagnetism; CSL is the chiral magnetic soliton phase; PM is the paramagnetic state; and FMM represents the forced ferromagnetic state).